Leibniz Association

Final report

Mixing And Transport in the Mesosphere and Lower Thermosphere (MATMELT)

Leibniz-Institute: IAP
Reference number: SAW-2014-IAP-1
Project period: 01.07.2014 – 30.06.2018
Contact partner: Erich Becker, Franz-Josef Lübken, Ralph Latteck

1 Introduction and main goals

The mesosphere and lower thermosphere (hereafter: MLT) is the atmospheric layer between about 50 km and 110 km altitude. This altitude regime is strongly controlled by waves that are generated at lower altitudes, and cause deviations from the (hypothetical) radiatively determined state by more than ± 100 K. The relevant wave types are internal gravity waves (GWs), traveling and stationary planetary Rossby waves (RWs), and thermal tides. All these waves are subject to dynamical instability, resulting into macro-turbulent cascades into smaller-scale waves and eventually into small-scale turbulence. In the MLT, atmospheric waves and turbulence are characterized by much higher amplitudes in terms of wind and temperature fluctuations than at lower altitudes. Therefore, the fundamental dynamics of the cascade processes can be studied much better here than in other regions of the atmosphere. Obtained results and new understanding, including the consequences for subgrid-scale (SGS) parameterizations in numerical models, are relevant for applications in the lower atmosphere and, in particular, for the formulation of weather and climate models.

It is important to acknowledge that the science community faces fundamental difficulties to formulate adequate subgrid-scale (SGS) parameterizations for atmospheric circulation models. This so-called *closure problem* is particularly relevant for the simulation of trace gases that are not well mixed (such as water vapor, ozone, odd nitrogen, atomic oxygen, metal layers in the MLT etc.). The reason is that on average, minor constituents (tracers) are not only *transported* by some Lagrangian mean flow (known as the residual circulation), but are also mixed. In models, the mixing results from the SGS diffusion in the tracer equation, and additionally by waves. In other words, the mixing of tracers in models depends crucially on both the SGS scheme and the resolved waves. For example, regarding the parameterization of GWs in conventional middle atmosphere climate models, the mixing by small-scale turbulence is accounted for, but the mixing that is directly due to the GWs is usually ignored.

This project has focused on the dynamical coupling across scales in the MLT and implications for *closure problem* in atmospheric circulation models with particular emphasis on the consequences for the dynamics of minor constituents (other equivalent words are trace gases or tracers). In addition, we focused on specific dynamical processes in the MLT (experimentally and theoretically) that are relevant for transport and mixing of trace gases. This reseach effort had a strong modeling and a significant observational component.

2 Progress, technical developments, and geophysical results

2.1 High-resolution global modeling using the KMCM

During the course of the project, the Kühlungsborn Mechanistic general Circulation Model (KMCM) has been further developed regarding the horizontal and vertical resolution, the SGS parameterizations, and the explicit simulation of GWs from orographic sources.

The KMCM is a free-running GCM based on a standard spectral dynamical core. It uses a terrain-following vertical coordinate. The current version employs a triangular spectral truncation at total horizontal wavenumber 240 and 190 full model layers (T240L190). The spectral truncation corresponds to a shortest resolved horizontal wavelength of 165 km (or a grid-spacing of 55 km). The vertical level spacing is ~ 600 m between the boundary layer and 3×10^{-4} hPa ($z \sim 100$ km). The level spacing increases in the lower thermosphere, and the highest model layer is located at 1.5×10^{-5} hPa ($z \sim 135$ km). This high spatial resolution is combined with an advanced parameterization of subgrid-scale diffusion according to Becker (2009) and Brune and Becker (2013) to describe GWs and their nonlinear interactions explicitly. The sponge layer of the KMCM is formulated as a linear harmonic horizontal diffusion that is applied above ~ 100 km and preserves angular momentum and energy (Becker, 2017). Furthermore, we include explicit computations of radiative transfer and the moisture

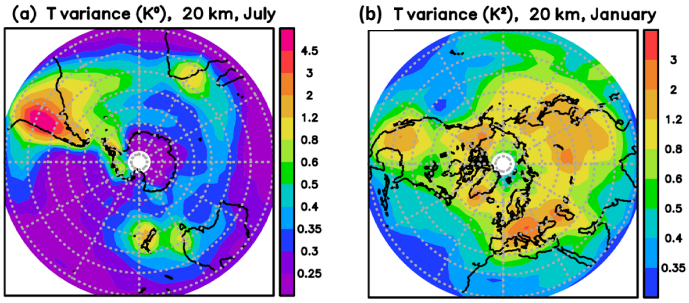

Figure 1: (a) Temperature variance at 20 km due to resolved GWs (horizontal wavelengths from 165 km to 2000 km) in the southern hemisphere during July, (b) same as (a), but for the northern hemsiphere during January

cycle, as well as simple parameterizations of thermospheric/ionospheric processes (see Becker et al., 2015; Becker, 2017). The surface energy budget is closed via a slab-ocean with prescribed lateral heat flux. The tracer transport in the KMCM is based on the spectral transform method, with a functional of the tracer being represented in spectral space such that the tracer is positive definite in grid space (Schlutow et al., 2014). This allows to simulate tracers consistently with the dynamics and the subgrid-scale diffusion. The Prandtl number for turbulent vertical diffusion is unity, but is set to Richardson number when this number exceeds unity. Such a constraint follows from the notion that the conversion of turbulent kinetic into turbulent available potential energy cannot exceed the turbulent shear production due to vertical momentum diffusion (see also Gassmann, 2018). The Prandtl number for molecular diffusion is unity, and all Schmidt numbers (for tracers like water vapor) are assumed to be unity.

No GW parameterization is used in the high-resolution KMCM. To date, there exist only two other GCMs that extend into the lower thermosphere and simulate semi-realistic GW effects in the mesopause region explicitly and with adequate spatial resolution: The JAGUAR model (Watanabe and Miyahara, 2009), and a high-resolution version of the WACCM (Liu et al., 2014).

The tropospheric sources of the resolved GWs in a general circulation model (GCM) are due to spontaneous emission, imbalances resulting from parameterized convection, and orography. As shown by Becker and Vadas (2018), the orographic GWs in the southern winter stratosphere make up for about half of the momentum flux in the stratosphere at middle and high latitudes. Figure 1 shows global stereographic projections of the simulated GW hotspots in the lower stratosphere during wintertime in terms of the GW-related temperature variance and vertical flux of zonal momentum. The relevant orographic hotspots in the SH are captured. Also the simulated GW hotspots in the NH are consistent with observational and modeling results (see Geller et al., 2013).

As shown in Becker and Vadas (2018), the large-amplitude *secondary GWs* in the southern winter MLT have a significant effect on the circulation. This is illustrated in Fig. 2, which shows the simulated zonal-mean climatology averaged from June 21 to August 10 and from December 21 to February 10 for the new GW-resolving version of the KMCM. The zonal wind and temperature (colors in Fig. 2) compare reasonably well with results from GCMs with GW parameterization, except for the polar winter mesopause region, which is characterized by an additional eastward wind maximum in either winter hemisphere (marked by additional red contours in Fig. 2 b,d). The black contours in Fig. 2 show the residual mass streamfunction and the resolved GW drag. Both fields are quantitatively consistent with results from GCMs with GW parameterization, except for the eastward GW drag centered around 60° and 3×10^{-4} hPa ($\sim$100 km) during winter. This eastward drag gives rise to residual upwelling over the winter pole from 10^{-3} hPa to 10^{-4} hPa ($z\sim$90 km–110 km). This leads to a decrease of the temperature with increasing latitude and explains the additional zonal wind maxima. Although no data is available to verify this feature, we note that GCMs with GW parameterization yield a reversal from eastward to westward flow in the winter MLT above $\sim$70 km and poleward of $\sim60^\circ$ latitude, while observational data show eastward flow on average in that region.

The simulated secondary GWs result from imbalances in the stratopause region generated by the intermittent body forces due to the breakdown of GWs having tropospheric sources (primary GWs).

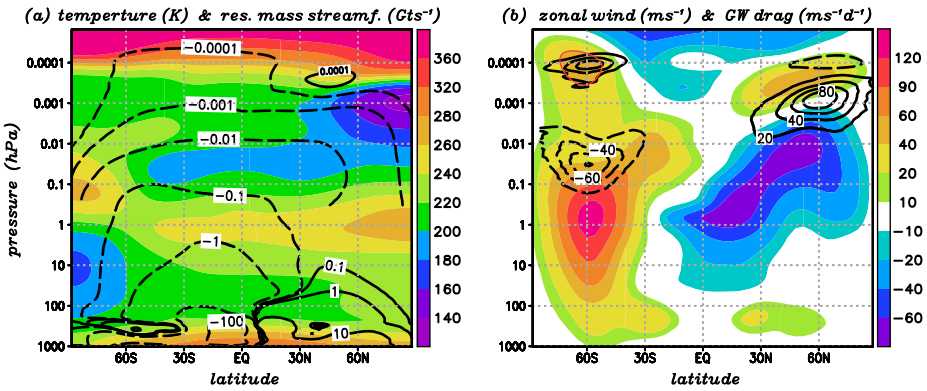

Figure 2: Zonal-mean climatology simulated with the KMCM during June 21 to August 10 (a-b): (a) Temperature (colors) and residual mass streamfunction (contours for $\pm 0.0001, -0.001, -0.01 \times 10^9$ kg s^{-1} above 0.3 hPa and for $\pm 0.1, \pm 1, \pm 10, -100 \times 10^9$ kg s^{-1} farther below) during June 21 to August 10, (b) Zonal wind (colors) and resolved GW drag (contours for $\pm 20, \pm 40, \pm 60, \pm 80$ m s^{-1}d^{-1}) June 21 to August 10. The GW drag is calculated as the EPF divergence for all waves minus the same quantity for waves with wavelengths longer than 1350 km only. The red 40 m s^{-1} contour marks the additional wind maximum in the southern mesopause region. The displayed altitude regime reaches from the surfaces to $\sim$130 km.

This coupling mechanism was studied in several papers with focus on the southern hemisphere (Becker and Vadas, 2018; Vadas and Becker, 2018; Vadas et al., 2018). Figure 2 indicates that secondary GWs are relevant in both hemispheres during wintertime in the MLT. Secondary GWs are ignored in conventional models where GWs are parameterized. In the following sections we show that the new discovery of secondary GWs has far reaching consequences for transport and mixing in MLT.

2.2 Turbulent parameters in the MLT: Annual cycle and secondary GWs

In a recent study we explored the role of GWs for GW amplitudes and turbulent parameters. The theory part of this work exploits the fact that the turbulent diffusion scheme in the KMCM is formulated in a hydrodynamically consistent way (which is not usual in models). More specifically, the entire momentum diffusion in the KMCM is based on a symmetric tensor, including a weak hyperdiffusion in order to simulate reasonable energy spectra (Brune and Becker, 2013). This allows to close the energy budget by applying the turbulent shear production as diabatic heating rate in the model's sensible heat equation. Since the kinetic energy is mainly dissipated by the nonlinear Smagorinsky scheme, the shear production is positive definite, as is required by the second law. Using a newly developed theory (Avsarkisov et al., 2019), we can derive small-scale turbulent parameters such as the Ozmidov scale, L_O, or the RMS turbulent velocity for Kolmogorov turbulence (KT). We also derived different kinds of Reynolds numbers and Froude numbers related to the transition from the buoyancy subrange to KT in the MLT by extrapolating the KMCM results using the aforementioned new theory. This transition was also analyzed in detail by Avsarkisov and Strelnikov (2019) based on rocket measurements, and a new turbulent regime was discovered. In the following we mention some highlights of the research based on the KMCM.

In a statistical mean, mesoscale structures in the MLT ($\sim$1 km to several 100 km) can be considered as a macro-turbulenct regime, sometimes also referred to as the buoyancy subrange (e.g., Lübken, 1997). A m^{-3} kinetic energy spectrum is typically observed, where m is the vertical wavenumber. This spectral behavior is often interpreted to arise from a superposition of saturated gravity waves GWs. Here, we follow ideas of Lindborg (2006) and denote this macro-turbulent regime as stratified macro-turbulence (SMT).

Classical theory of KT postulates that if L and U are the integral length scale and velocity of turbulent eddies, then a proper timescale is $\tau = L/U$. This means that the energy of eddies of size $L \sim k^{-1}$ and velocity U is cascaded to smaller scales during time τ. This time scale is sometimes

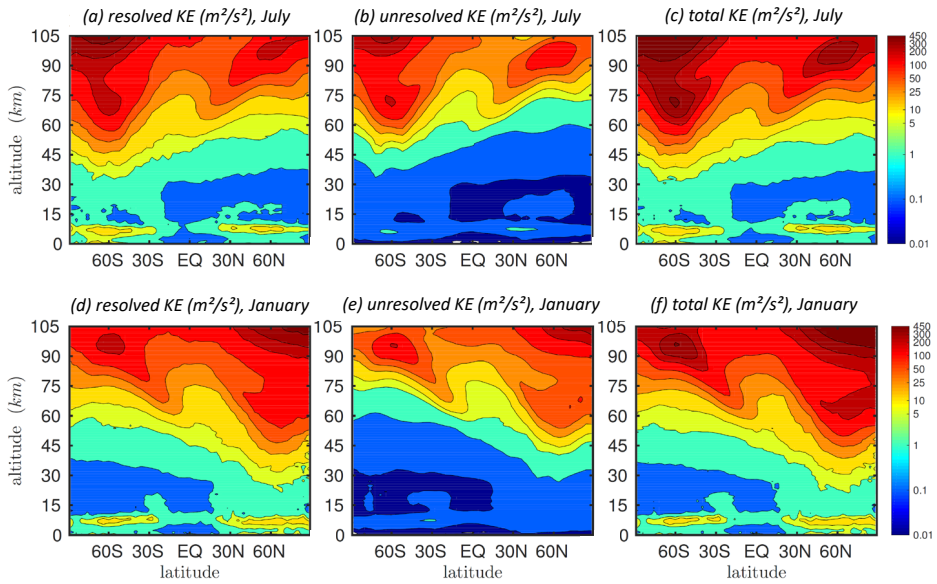

Figure 3: Zonal-mean climatology of the kinetic energy during July (upper row) and January (lower row) as simulated with the KMCM. Shown are the macroturbulent kinetic energies per unit mass (KE) from the resolved flow (horizontal wavelengths from 165 km to 1000 km), from the unresolved flow (i. e., from the subgrid scales), and the sum of the two.

also referred to as the eddy turnover time. Assuming a scale-independent spectral energy flux, this flux must be balanced by the dissipation, i. e., by the rate at which kinetic energy is irreversible converted into heat by molecular viscosity, denoted as ϵ. Using $E_k \sim U^2$, this balance can be expressed as $\epsilon \sim E_k/\tau \sim E_k^{3/2}/L$. This leads to the well-known $k^{-5/3}$ law for the kinetic energy spectrum, e_k, which is related to integral-scale kinetic energy via $E_k \sim \int_k^\infty e_{k'} dk'$. Introducing a turbulent viscosity at scale L, $\nu_t \sim L\,U$, the dissipation rate can be written as $\epsilon \sim \nu_t\, U^2/L^2$, and the integral kinetic energy at scale L as $E_k \sim \sqrt{\nu_t \epsilon}$. In Large Eddy Simulations (LES) of KT (i. e., with the numerical truncation scale somewhere between the inner and outer scale of KT), the last equality can be used to diagnose the kinetic energy of the unresolved scales. When using the k-ϵ model as SGS parameterization, the relation

$$E_{SGS} \sim \sqrt{\nu_t \epsilon / c} \tag{1}$$

applies, where $c \approx 0.09$. In the following we derive a corresponding relation to diagnose the unresolved kinetic energy from the high-resolution KMCM.

We define L_h and L_v as the characteristic horizontal and vertical scales of the flow in the buoyancy subrange; U_h and U_v are the corresponding horizontal and vertical characteristic velocities. While $U_v \sim U_h$ and $L_v \sim L_h$ for KT, we have $U_h \gg U_v$ and $L_h \gg L_v$ for SMT. We assume that SMT applies for scales that are larger than the outer scale of KT (which is approximately given by L_O) and smaller than the synoptic scale for quasi-geostrophic flow. Since horizontal divergence and relative vorticity are about of the same order of magnitude for SMT, we have $U_v/L_v \sim U_h/L_h$. Furthermore, SMT is subject to the scale-dependent aspect ratio (e.g., Brune and Becker, 2013): $L_v \sim \epsilon^{1/3}\, N^{-1}\, L_h^{1/3}$, where N is the background buoyancy frequency. The integral kinetic energy in this regime can be approximated by U_h^2. Furthermore, we take advantage of the fact that the forward kinetic energy cascade in SMT is strongly due to the horizontal advection terms. According to these arguments, a generalization of Eq. (1) to the regime of SMT yields

$$E_{h\,SGS} \approx \sqrt{\nu_{ht} \epsilon_h / c}\,. \tag{2}$$

Here, the SGS kinetic energy is mainly due to the non-resolved horizontal winds in the SMT regime, and ν_{ht} and ϵ_h are the horizontal momentum diffusion coefficient (abbreviated as K_h in our previous

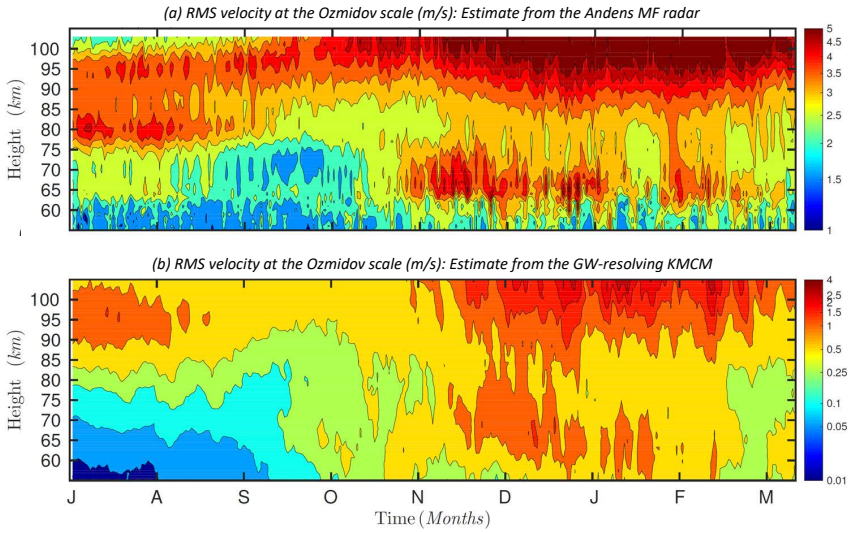

Figure 4: Estimates of the RMS velocity at the Ozmidov scale (corresponding to the outer scale of KT) from the MF radar at Andenes and from KMCM at the same site

papers) and the frictional heating (macro-turbulent shear production) owing to horizonal momentum diffusion, respectively.

Figure 3 shows the resolved, unresolved (SGS), and total macro-turbulent kinetic energies (KE) as simulated by the KMCM for July and January. The resolved KE in the mesoscales (panel a and d) is diagnosed as the kinetic energy from the full spectral expansion up to total horizontal wavenumber 240, minus the kinetic energy for spectral truncation at wavenumber 40. The resulting mesoscale kinetic energy (KE) then consists of contributions from wavenumber 40 to 240 only, corresponding to horizontal wavelengths from 1000 km down to 165 km. The unresolved KE is computed from Eq. (2) and shown in Fig. 3 b and e. Adding this SGS kinetic energy to the resolved KE gives rise to the total KE contained in horizontal wavelengths shorter than about 1000 km (panels c and f).

Comparing the different energies in Fig. 3 we see that the diagnosed non-resolved (SGS) KE is quite significant in the middle atmosphere, though being somewhat smaller than the resolved part. Interestingly, its structure matches with that of the resolved KE. The reason is that the latter reflects the resolved GWs, and that high GW amplitudes give rise to enhanced momentum diffusion and wave-mean flow interaction (GW drag and dissipation of resolved GW kinetic energy). As a result, the maxima of the total KE are even more pronounced than the maxima of the resolved mesoscale kinetic energy.

These maxima can be characterized as follows: There is a sudden onset of the KE with height above about 75 km in summer. This corresponds to fast eastward GWs generated in the troposphere which strongly grow in amplitude and dissipate as a result of the wind reversal from westward to eastward flow in the upper summer mesosphere (see Fig. 2. Note that in summertime, all westward and slow eastward primary GWs are filtered in the troposphere and lower stratosphere. In the winter middle atmosphere, on the other hand, all eastward primary GWs dissipate well below the polar night jet maximum, while westward primary GWs (including orographic GWs) generated in the troposphere dissipate in the stratopsphere and lower mesosphere (depending on their amplitudes, scales, and horizontal phase speeds). As a result, both the resolved and unresolved KE are much stronger in the stratosphere and lower mesosphere during wintertime than during summertime. This winter-summer asymmetry is also evident in the mean turbulent dissipation rates as deduced from rocket measurements (Lübken, 1997).

Note that the largest GWs amplitudes and dissipation rates are found in the winter polar mesopause region (around 100 km height). According to Becker and Vadas (2018), this maximum is mainly due to secondary GWs that are generated in the stratopause region due the imbalances that result from the intermittent body forces associated with the breakdown of the primary GWs. Indeed, secondary

GWs are responsible for the strongest GW activity in the terrestrial atmosphere. Moreover, this feature is absent in comprehensive community climate models due to parameterization of GWs.

The characteristic velocity at the Ozmidov scale corresponds to the characteristic integral velocity or the turbulent root-mean-square (RMS) velocity of the KT regime. This velocity can be deduced from the KMCM results by appying scaling arguments from turbulence theory (Avsarkisov et al., 2019). The same velocity is also known as the RMS velocity that can be deduced from ground-based MF radar measurements using full correlation analysis Reid (2015).

IAP operates an MF radar in Northern Norway near the city of Andenes. The radar is located near the polar circle (69°N, 17°E) and therefore measures winds and wind fluctuations in the regime where we expect maximum secondary GWs amplitudes during wintertime. More information about the radar is given in Wilhelm et al. (2017). Using the methods reviewed by Reid (2015), the RMS velocity at the Ozmidov scale can be estimated. Figure 4 a shows the result for the annual cycle of the RMS velocity from the MF radar. The overal structure, with the strongest maximum in the winter mesopause region, is consistent with model results shown in Fig. 3. Though the model estimate generally predicts smaller values for the RMS velocity (the radar method is known to overestimate the RMS velocity), both methods agree on the double maximum during wintertime, with enhanced turbulence around 60 km – 70 km (from the dissipation of primary GWs) and above 90 km (from the dissipation of secondary GWs). A similar result was also reported by Reid (2015). From our recent model studies based on the KMCM we now can explain this structure.

2.3 Downward mixing of NO_x through the winter mesopause

Due to energetic particle precipitation (EPP) being focused into the polar caps the polar upper mesosphere and lower thermosphere is a permanent source of odd nitrogen ($NO_x = NO + NO_2$). The thermospheric NO_x is transported downward across the winter polar mesopause and can lead to significant ozone destruction in the middle atmosphere on a seasonal time scale (EPP indirect effect). Comprehensive whole atmosphere climate models fall short of simulating the necessary NO_x transport across the mesopause and the corresponding consequences on the middle atmosphere. The discrepancy is caused most likely by the lack of downward transport of NO_x across the winter polar mesopause.

As explained in the previous subsections, it is the polar winter mesopause region where the GW amplitudes and dissipative effects are strongest due to secondary GWs. The hemispheric differences simulated with the KMCM (see Fig. 3) suggest that secondary GWs are generally stronger in southern winter than in northern winter. However, secondary GWs can become very strong also in northern winter, namely in the wake of sudden stratospheric warmings (SSWs) when a strong polar vortex develops along with an elevated stratopause. It is precisely during such periods when the EPP indirect effect is usually observed in the northern hemisphere (Randall et al., 2009).

We propose that secondary GWs are the missing link mechanism in the transport of minor constituents across the winter mesopause in our understanding of the EPP indirect effect. As shown by Smith et al. (2011) using tracer transport calculations based on the Whole Atmosphere Community Climate Model (WACCM), minor constituents are transported downward from the winter polar mesosphere into the stratosphere, but enter the polar mesosphere exclusively due to meridional transport by the residual circulation from low to polar latitudes. Such a result would be obtained also with the GW-resolving GCM since the eastward GW drag by secondary GWs reduces or even reverses the downwelling in the winter polar mesopause region. Secondary GWs having large amplitudes and large scales nevertheless do lead to downward transport of NO_x. The corresponding mechanism has been known as *GW mixing*: The explicit consideration of GWs in the transport of tracers gives rise to a down-gradient mean tracer flux that occurs in addition to 1) the transport by the residual circulation, and 2) the tracer flux related to turbulent and molecular diffusivity. Grygalashvyly et al.

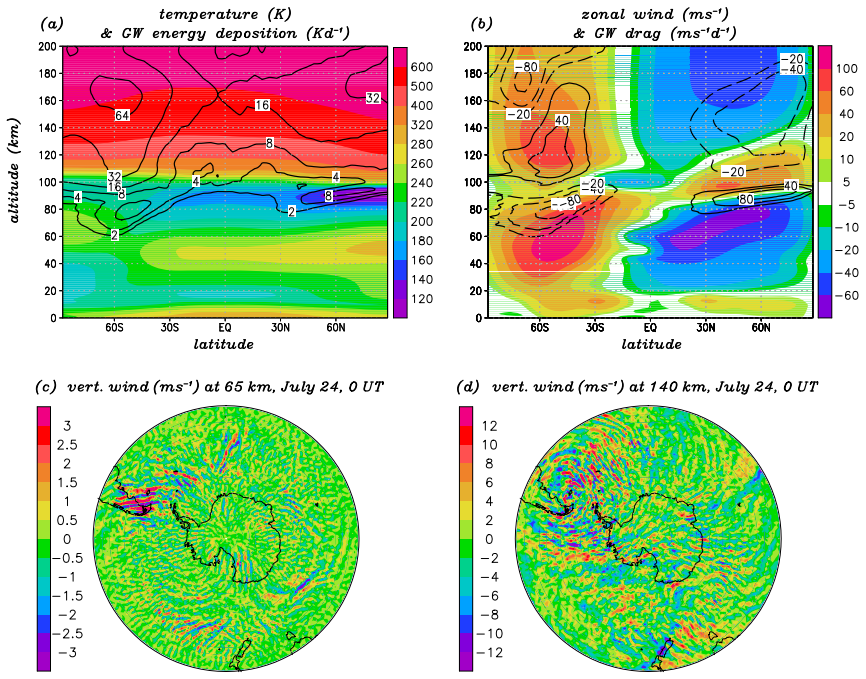

Figure 5: Simulation results from the KMCM T240L220 for July: (a) zonal-mean temperature (colors) and energy deposition by resolved GWs (contours for $2, 4, 8, 16, 32, 64$ K/d), (b) zonal-mean zonal wind (colors) and GW drag (contours for ± 20, $40, 80$ m/s/d. GW perturbations are computed using the spectral transform method, retaining only horizontal wavelengths shorter than 1350 km, (c),(d) Snapshots of the vertical wind at 65 km and 140 km

(2012) analyzed this mechanism using a chemistry-transport model in combination with a previous GW-resolving version of the KMCM.

Here we perform short-term simlations using an extended version of the new GW-resolving KMCM with 30 more levels and a model top is at 9×10^{-7} hPa corresponding to ~ 200 km. Figure 5 demonstrates that this model simulates reasonable zonal-mean winds and temperatures from the surface to the model top (colors in panel a and b). The strong reversals of the GW drag at middle to high latitudes in the thermosphere towards eastward in winter and westward drag in summer result from secondary GW generation in the winter lower mesosphere and in the summer mesopause region, respectively. In southern winter, there is even a second reversal of the GW drag above ~ 150 km which presumably results from tertiary GW generation in the thermosphere. The strength of the mean thermospheric GW drag and the GW energy deposition are comparable to corresponding contributions from thermal tides (not shown); they yields significant contributions to the momentum and heat budgets of the lower thermosphere. The resolved GW variations are huge. This is illustrated in Figs. 5 c and d by snapshots of the vertical wind over the southern polar cap at different heights. An orographic GW event is visible over the Southern Andes in panel c at 65 km. The secondary GWs emitted from this event show up as concentric rings in the lower thermosphere (panel d) downstream (to the east) of the source.

Figure 6 shows results during August for a tracer with a horizontally uniform (in pressure coordinates) initial condition that is maximum around ~ 120 km (panel a). Panel b shows a 6-hour average after 3 days of the simulation. The difference to the initial condition is also indicated by white contours for the tracer mass density. Generally, the tracer has been transported by the residual circulation, mixed by waves, and diffused by parameterized turbulence and molecular diffusivity. Comparing the two tracer distributions with the residual mass streamfunction (white contours in panel a), we can conclude that the tracer has been mixed upward above ~ 120 km, and that this effect is amplified in summer and reduced in winter by the residual circulation. In the mesosphere, the tracer is transported upward in summer and downward in winter by the residual circulation. The latter results in a strong enhancement of the tracer mass from about 50 km – 80 km over the winter pole. The reversed residual circulation at 80 km – 110 km in winter and at 90 km – 120 km in summer results from the reversed GW drag and the mean-flow effects from tides in this region. As a result, no tracer mass can be transported downward across the winter polar mesopause by the residual circulation.

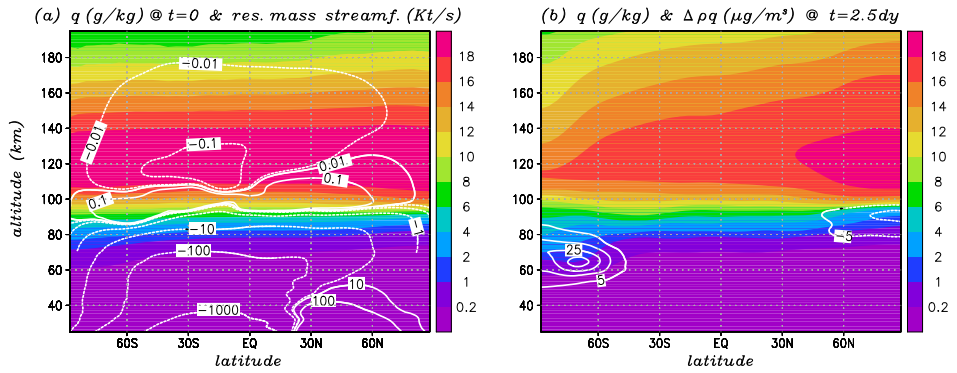

Figure 6: Tracer transport in the GW-resolving KMCM during July: (a) initial mass mixing ratio (colors) and residual mass streamfunction (averaged over 3 days of simulation, contours drawn for $\pm 0.01, 0.1, 1, 10, 100, 1000 \times 10^6\,\mathrm{kg\,s^{-1}}$), (b) zonal-mean mass mixing ratio after 3 days of simulation (colors, averaged over 6 hours). The difference to the initial condition is inserted in terms of the mass density (contours drawn for $\pm 5, 15, 25, 35 \times 10^{-9}\,\mathrm{kg\,m^{-3}}$).

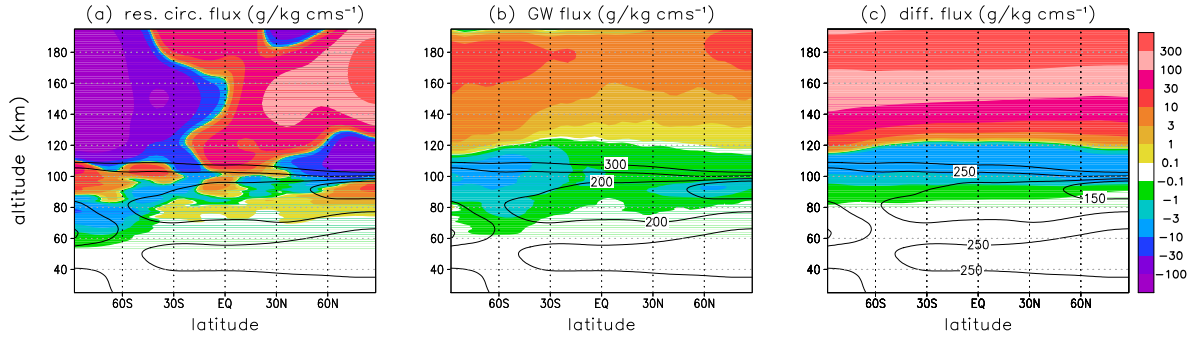

Figure 7: Vertical fluxes (colors) of a tracer in the GW-resolving KMCM during July due to (a) the residual circulation, (b) resolved GWs, and (c) diffusion (see text for further details). GW perturbations are computed using the spectral transform method and retaining only horizontal wavelengths shorter than 1350 km. For better orientation, the temperature field is included by a few contours (drawn for $150, 200, 250, 300\,K$).

The vertical tracers fluxes due to the residual circulation, mixing by GWs, and mixing by the SGS diffusion were averaged over the 3 days of the simulation (see Fig. 7). Both mixing fluxes are upward above $\sim$120 km and downward farther below, with the GW flux reaching down to the winter stratopause and amplifying the effect of the residual circulation. In particular, tracer mass is mixed downward across the winter polar mesopause. This mixing would be absent if GWs were parameterized, because large GW amplitudes and a strong turbulent diffusion coefficient around the winter polar mesopause are caused mainly by the secondary GWs.

2.4 Airglow simulations using a high-resolution chemistry transport model

We used the high-resolution model data from the KMCM with a model top at 135 km (Becker and Vadas, 2018) to drive our chemistry transport model (CTM) of the MLT (e.g., Grygalashvyly et al., 2011, 2012). An additional diagnostic tool for the computation of airglow (emission in the far infrared) from excited hydroxyl in the mesopause region was developed for the CTM (Grygalashvyly et al., 2014; Grygalashvyly, 2015). With this combination of models we investigated the influence of GWs on airglow.

This topic is highly important because airglow measurements are frequently used to infer temperatures in the mesopause region, including GW perturbations, annual cycle, and long-term changes. A constant emission height of $\sim$87 km is usually assumed in corresponding analyses of ground-based measurements. On the other hand, as is outlined farther below, our modeling results show that the instaneous airglow layer varies significantly due to GWs. In addition, we find that the mixing effect

due to GWs has significant effect on atomic oxygen, and this controls the average altitude of the emission from excited hydroxyl, particulary in polar winter due to secondary GWs. Corresponding results are currently being prepared for publication Becker et al. (2019), and are summarized below.

2.4.1 Chemistry-transport model (CTM)

Our CTM includes chemical reactions, radiation, transport, and subgrid-scale vertical diffusion. Our present simulations were performed on grid with 576 longitudinal and 286 latitudinal grid points, as well as 118 vertical levels in log-pressure coordinates from the ground to approximately 150 km, using a scale height of 7 km. This distribution of grid points in the CTM allows to take full advantage of all scales resolved by the KMCM. To drive the CTM, the pre-calculated dynamical fields are interpolated to the grid of the CTM.

The chemistry module consists of 19 constituents and includes 49 chemical reactions and 14 photodissociation processes. The reaction rates are calculated on-line. The chemistry module takes advantage of the family concept, considering odd hydrogen (H, OH, HO_2, H_2O_2), odd oxygen (O, O(1D), O_3), and odd nitrogen (NO, NO_2, N(4S), N(2D)) as families. Chemistry processes are computed with the implicit Euler scheme, including a quadratic loss term. The long-lived and short-lived constituents are solved separately, where the short-lived constituents are included in the chemical families, which are solved as fully implicit subsystems. The CTM uses fixed absorber concentrations for the calculation of the photodissociation rates. The dissociation rates in the model are taken from a pre-calculated library and depend on height and zenith angle. The transport is calculated according to Walcek (2000). The vertical diffusion includes both turbulent and molecular diffusivity. For the turbulent diffusion coefficient we employ a fixed vertical profile for all horizontal gridpoints that is based on the results of Lübken (1997).

In order to derive the excited hydroxyl (OH^*) number density for a given vibrational level we assume that OH^* is in photochemical equilibrium. Thus, we can calculate the number density of OH^* and the associated emission rate from the ratio of the sum of all production terms to the sum of all loss terms. The production includes the production of OH^* 1) from the reaction of atomic hydrogen with ozone, 2) from the reaction of hydroperoxy with atomic oxygen, and 3) from transitions from the highest vibrational level to lower levels due to quenching (by atomic oxygen, molecular nitrogen, and molecular oxygen). In addition to the losses due to quenching, we include spontaneous emission and the reaction of excited hydroxyl with atomic oxygen as loss processes. Since the study of Grygalashvyly et al. (2014), our airglow model has been further developved by including multi-quantum quenching by atomic oxygen. Further information about the CTM and the coupled airglow model can be found in Grygalashvyly et al. (2011, 2012, 2014) and Grygalashvyly (2015).

2.4.2 Instantaneous variations of the airglow layer induced by GWs

Figure 8 shows the typical result for the variations of the airglow emission layer from vibrational number $\nu = 6$. Evidently, the vertical wind variations due to GWs which are of the order of several m/s in our high-resolution GCM (panel b), are associated with variations in the temperature (panel) and atomic oxygen (panel c). Note atomic oxygen is strongly controlled by dynamics at mesopause altitudes and therefore subject to dynamical effects associated with GWs, including instantaneous transport and averaged mixing (Grygalashvyly et al., 2012). Grygalashvyly (2015) derived an approximate formula for the concentration of OH^* that illustrates the strong control of the emission layer by the concentration of atomic oxygen. Hence, the GW-induced variations of atomic oxygen can explain most of the instantaneous variations of $OH^*_{\nu=6}$ in Fig. 8 c. Variations of $OH^*_{\nu=6}$ are also generated since the reactions and transition considered in the prodcution and loss terms depend on the temperature. Currently it is not known which process is most important. It is clear, however, that the airglow layer is by no means constant in altitude and undergoes significant variations even

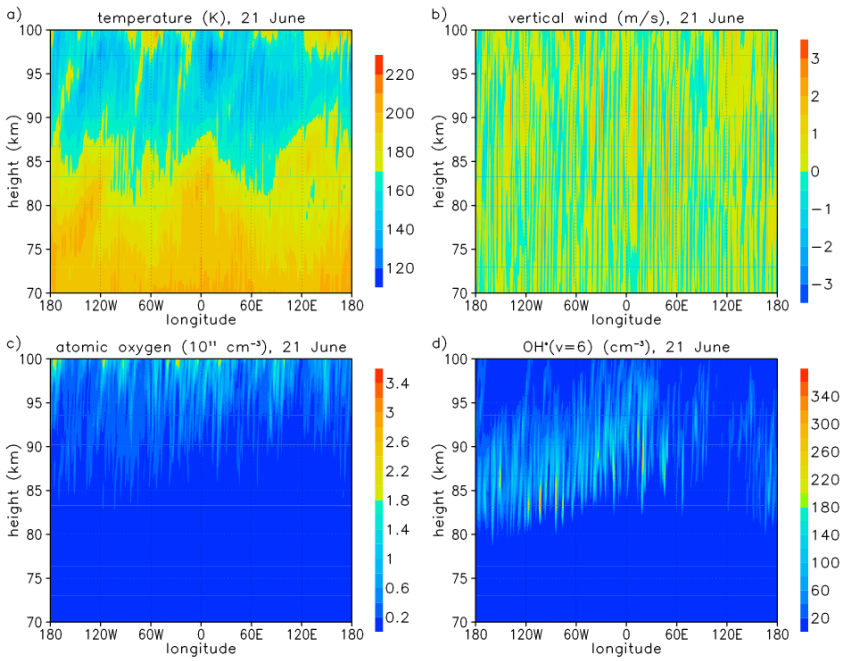

Figure 8: Snapshot illustrating the longitude-height variation of a) temperature, b) vertical wind, c) atomic oxygen number density, and d) $OH^*_{\nu=6}$ concentration at 54°N during summer solstice. Simulation result from the CTM driven by the GW-resolving dynamical fields from the KMCM. The vertical coordinate is the log-pressure height, assuming a scale height of 7 km. Note that in the region of the summer mesopause the (true) geometric height is about 5 km less than than the log-pressure height.

on spatial and temporal scales associated with GWs. Other variations with latitude and season in the tropics and subtropics are known from satellite measurements (von Savigny, 2015). According to our model results, such variations extend also to higher latitudes (not shown).

2.4.3 GW mixing effect on the airglow layer

The effect of GW mixing on the airglow shows up either in the zonal or in the temporal mean. Figure 9 shows results from a sensitivity experiment. That is, in addition to our control simulations we run the CTM with the same large-scale dynamical fields from the KMCM, but filtered all GWs having horizontal wavelengths short than 1000 km. The upper panels in Fig. 9 show the zonal-mean concentrations of atomic oxygen and $OH^*_{\nu=6}$ for this CTM simulation. The lower panels show the model response of the CTM when the full dynamical fields of the KMCM are used to the CTM. In other words, the lower panels show the differences between the results from the control simulation and the additional CTM simulation without GWs. We can see that GWs lead to significant downward mixing of atomic oxygen. Due to the aforementioned control of the airglow layer by atomic oxygen, this leads to a corresponding downward shift of the nighttime airglow layer of more than 5 km at high latitudes in the southern winter mesopause region. Similar results are obtained for the northern hemisphere during polar winter (not shown). This influence is solely a result of the mixing of minor constituent by GWs. It is similar to the downward mixing of NO_x in the polar winter mesopause region discussed in Sec. 2.3. We conclude that the recent discovery of secondary GWs leading to the strong GW in the polar winter mesopause region has also significant consequences for our understanding of mean alitudes of the airglow layer in polar winter.

2.5 Winds, transport, and mixing from satellite data analysis

One aim of the project MATMELT was to extend and optimize the method to derive daily-mean wind fields and mixing in the stratosphere and mesosphere from Aura-MLS satellite data (provided by NASA), using temperature, geopotential and trace gas concentrations as input. In high altitude

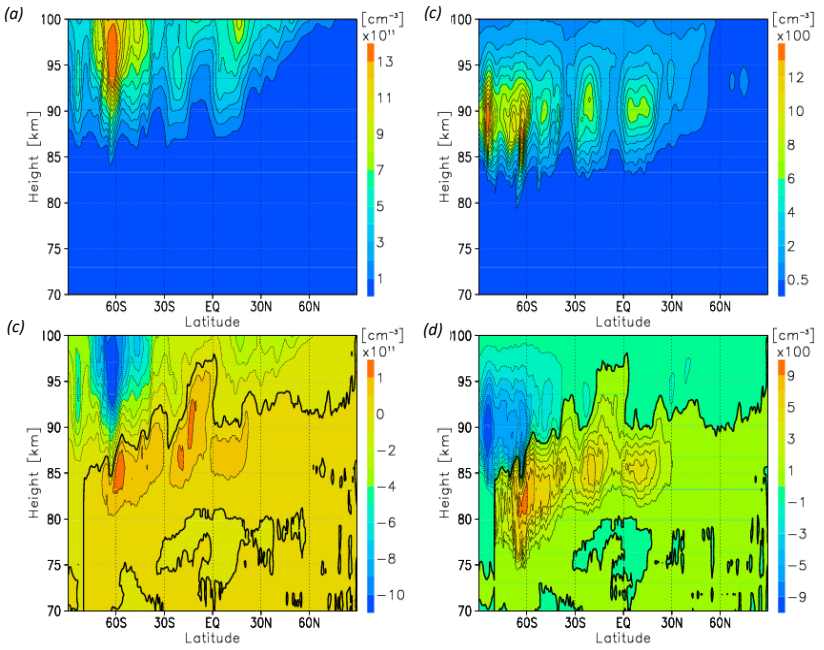

Figure 9: (a) Zonally averaged concentration of atomic oxygen at summer solstice for the simulations when the CTM is driven by only the large dyanmical fields from the KMCM down to horizontal wavelengths of 1000 km. (b) Model response when the full dynamical fields, including GWs down to horizontal wavelengths of 165 km are used to drive the CTM. (c) and (d) Same as (a) and (b), respectively, but the zonally averaged concentration of $OH^*_{\nu=6}$. The vertical coordinate is the log-pressure height like in Fig. 8.

models, the simulated winds, and the associated transport and mixing, are still highly uncertain. One reason is the lack of validation with direct wind measurements between 30 km and 80 km (e. g., Baron et al., 2013).

In a preliminary work we derived winds from temperature and geopotential using standard balance equations subject to quasi-geostrophic scaling (these winds included the balanced ageostrophic components, i. e., vortical and non-vortical flow, as well as vertical winds). Results showed that the transport and mixing by large-scale waves derived from these balanced winds can explain only a fraction of the observed stationary wave patterns in stratospheric ozone (O_3) and stratospheric and mesospheric water vapour (H_2O). The strongest deficits occur in the mesosphere where unbalanced winds play a major role in transport and mixing (Gabriel et al., 2011; Demirhan Bari et al., 2013). Therefore we developed a new optimization method that iteratively adjusts the transport and mixing, taking advantage of the fact that H_2O is a nearly inert tracer in the stratosphere and mesosphere. More specifically, we adjust the daily-mean wind vectors by iteratively adjusting the advection in the transport equation for H_2O such that the observed day-to-day variations in H_2O are reproduced optimally by a transport model. This algorithm involves an inversion of the tracer transport equation, and it includes SGS mixing in terms of a simple Gaussian grid-point filter.

We write the final result of the daily-mean wind vector as $\mathbf{v} = \mathbf{v}_b + \mathbf{v}_c$. Here, $\mathbf{v}_b$ is the balanced wind and $\mathbf{v}_c$ is the correction resulting from the optimzation. Figure 10 shows an example for monthly-mean vertical winds, indicating a contribution of 30 % from the correction w_c to the total vertical wind $w_b + w_c$. The correction depends on the time interval that is considered. For example, on a daily-mean basis the corrections can easily exceed 50 %, while the monthly-mean corrections are small. Figure 10 also shows that the corrections are pronounced in the upper stratosphere and in the mesosphere.

The aforementioned representation of mixing in terms of grid-point filtering is not very physical (though applied in many models). Therefore, as a further step, we introduced explicit eddy mixing in our algorithm. This is done via an explicit diffusivity tensor that is computed from an additional

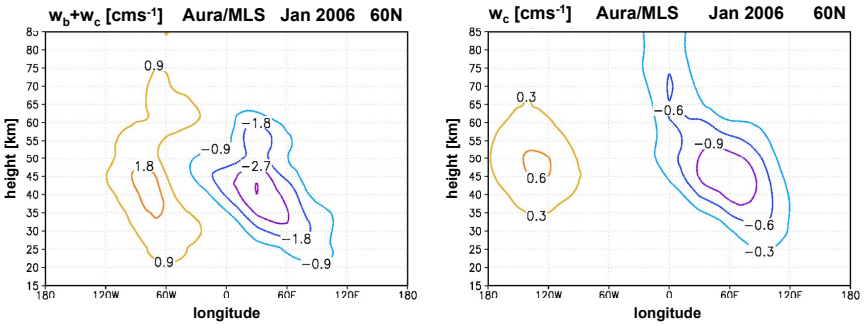

Figure 10: Monthly-mean vertical winds at 60^{o}N in January 2006 derived from Aura/MLS.
Left: Total wind ($w_b + w_c$, balanced plus unbalanced component).
Right: Unbalanced component.

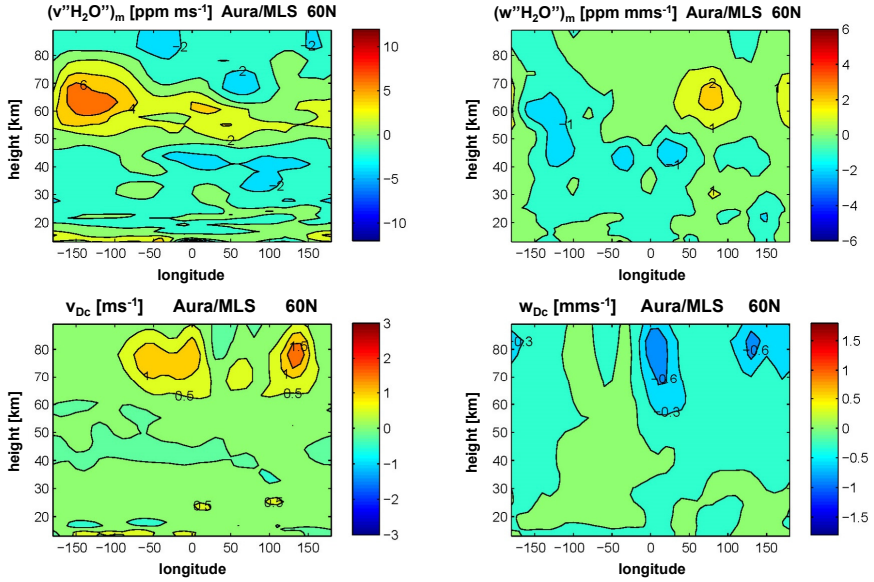

Figure 11: Upper panels: Monthly means of meridional and vertical subgrid-scale eddy fluxes of H_2O as computed from the transport budget. Lower panels: Meridional and vertical wind corrections resulting from the iterative adjustment when including the subgrid-scale eddy fluxes. Results are for 60^{o}N in January 2006.

optimization of the monthly-mean transport budget. To this end, we complete the advection of water vapor density by the monthly-mean wind and water vapor fields, $\nabla \cdot (\mathbf{v}_m \mu_m)$, 1) by resolved eddy fluxes, $\nabla \cdot (\mathbf{v}'\mu')_m$, where $\mathbf{v}'$ and μ' are the daily deviations from the monthly means, and 2) by the advection due unresolved scales, $\nabla \cdot (\mathbf{v}''\mu'')_m$, where $\mathbf{v}''$ and μ'' are the unknown SGS daily deviations. That is, we require that $\nabla \cdot (\mathbf{v}'\mu')_m + \nabla \cdot (\mathbf{v}'\mu')_m + \nabla \cdot (\mathbf{v}''\mu'')_m = 0$ for the monthly-mean advection of water vapor. The SGS mixing is parameterized by a symmetric diffusivity tensor. This tensor is updated each iteration step along with the daily-mean wind field. Very good convergence (less than 1 % changes between two steps) is obtained below about 70 km after about 30 iterations. We denote the obtained corrections to the wind field by $\mathbf{v}_{Dc}$ (as opposed to $\mathbf{v}_c$ for the algorithm without explicit SGS diffusion).

As an example, Figure 11 shows the monthly means of the SGS merdional and vertical eddy fluxes (upper panels) and the corrections in the meridional and vertical wind components (lower panels). The patterns are generally consistent with the usual picture of the time-mean circulation and transport, i. e., eddy mixing fluxes can partly offset the transport by the large-scale flow, but it can occasionally also act in the same direction. We obtain poleward ($v_{Dc} > 0$) and downward ($w_{Dc} < 0$) mixing in the northern winter mesosphere as an important component of the mean transport. More comprehensive results are currently being published Gabriel (2019).

Still some uncertainties of the method have to be considered. For example, an iterative inversion procedure is strongly dependent on a meaningful initial first guess. Below $\sim$70 km such a guess is given by the balanced winds, and we obtain a very good convergence of the iteration method. At higher altitudes our iteration results are sensitive to the initial diffusivity. We are currently working on solutions to this problem.

2.6 Radar measurements

Ground-based measurements from winds have been derived from two unique radar systems: (a) the Middle Atmosphere Alomar Radar System (MAARSY), and (b) different variants of the Multi-statistic Multi-frequency Agile Radar Investigations Atmosphere (MMARIA) systems. Briefly, the MAARSY system allows wind measurements of the polar summer mesosphere with an area of 30 km x 30 km around 80 km altitude with temporal, altitudinal, and horizontal resolutions of 5 min, 300 m, and 5 km, respectively (e.g., Stober et al., 2018b). On the other hand, MMARIA applied to specular meteor radars (SMRs) allows to infer horizontal wind fields over areas of $\sim$400 km x 400 km, with lower temporal, altitude and horizontal resolutions than MAARSY (i. e., 1 hour, 2 km, and 15 km, respectively) (e. g., Stober and Chau, 2015; Chau et al., 2017; Stober et al., 2018a). In the following we summarize our geophysical results.

2.6.1 Gravity waves and Kelvin-Helmholtz instabilities at the polar summer mesosphere

The MAARSY system has been used on special multi-beam mode to study temporal and spatial features of waves using polar mesosphere summer echoes (PMSE) as tracers of the neutral dynamics. A campaign was conducted for nine days in June 2013 with 67 different beam positions (see lhs panel in Figure 12). During this time, we have identified two Kelvin-Helmholtz instability (KHI) events from the signal morphology of PMSE. Those events were characterized by horizontal separations of 8 km to 12 km. Background neutral wind during this campaign have been obtained from collocated SMR measurements. Such measurements provided gravity wave (GW) activity and altitudinal profiles of the background horizontal winds (above and below the PMSE region). The KHIs occurred in a strong shear flow with Richardson numbers $R_i < 0.25$. Our KHI results suggest that GW wave packets may undergo a significant acceleration in their phase speeds when propagating upward, reaching different background flows and evolving into different forms of instabilities. Other mesospheric observations indicated that wave ducting can lead to waves propagating with high phase speeds.

In addition, we observed 15 wave-like events in our MAARSY multibeam observations, after removing the effects of the background wind on the measured radial velocities. From the 15 identified monochromatic waves, we retrieved the horizontal wavelength, intrinsic frequency, propagation direction, and phase speed. These events showed horizontal wavelengths between 20 km and 40 km, vertical wavelengths between 5 km and 10 km, and rather high intrinsic phase speeds between 45 m/s and 85 m/s with intrinsic periods of 5 min to 10 min. The rhs panel in Fig. 12 shows a histogram of occurrence of these waves in a polar diagram (blue). The mean flow direction is indicated in red. The observed values are in reasonable agreement with model simulations of breaking mesoscale GWs generated from convective tropospheric clouds. More details can be found in Stober et al. (2018b).

2.6.2 Mesospheric mean vertical wind during the polar summer

During the summer the polar mesospheric mean vertical wind is expected to be positive, consistent with the well accepted mean residual circulation with values in the order of a few cm/s. However, direct measurements and confirmation of such values have not been possible in the past given the difficulty to sample the region continuously, the high amplitudes of the vertical fluctuations, and the expected small mean value. Recently, we have been able to infer such mean positive winds from measreuments. The first evidence was obtained from horizontal divergence measurements using the MMARIA approach to two closely located SMRs (Andoya and Tromso, respectively) (Chau et al., 2017). Evidence was also derived from a careful analysis and processing of PMSE vertical velocities. Using measurement uncertainties as weights to obtain seasonal weighted averages vertical velocities, the seasonal mean vertical velocities were characterized. Weighted average values of vertical velocities reveal a weak upward behavior at altitudes 84 km – 87 km after eliminating the influence of ice falling speed, as expected. At the same time, a sharp decrease/increase in the mean vertical velocities at the

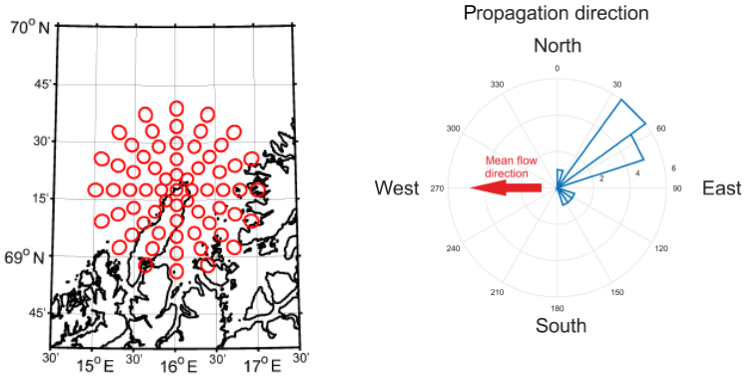

Figure 12: Left: Projection of MAARSY beam positions; the red circles show the illuminated radar beam area at 84 km altitude. Right: Polar diagram of wave propagation direction; the red arrow denotes the mean wind direction.
(From: Stober et al., 2018a).

lower/upper edges of the summer mean altitude profile prevails, which are attributed to the sampling issues of PMSE due to disappearance of the target corresponding to certain regions of motions and temperatures (Gudadze et al., 2018).

2.6.3 Comparisons of mesospheric winds and tides with KMCM

Thermal tides play an important role in the global atmospheric dynamics and provide a key mechanism for the forcing of thermosphere-ionosphere dynamics from below. Multi-year observations of mesospheric winds and tides from ground-based SMRs, located in northern Germany and Norway, were analyzed to obtain a climatology. The observed seasonal variability of the tides was compared to long-term simulations performed with the Kühlungsborn Mechanistic general Circulation Model (KMCM) (Becker, 2017). The simulated tides show similar behaviour as the radar-observed tides. In particular, the highest amplitudes occur in winter and during the fall transition. We also find stronger tidal amplitudes at middle than at high latitudes. Furthermore, tidal amplitudes of the meridional wind is stronger than that of the zonal wind. This feature is also similar in the observations and in the model data. These results were presented and discussed in Pokhotelov et al. (2018). We also noticed significant differences between the observed and simulated tides. To understand these difference requires further examinations of the model data regarding the mean flow and the interaction of gravity waves and tides.

2.7 Lidar measurements

2.7.1 Fe Lidar

The mobile Fe lidar of the IAP is the only transportable Doppler resonance lidar for temperature measurements in the mesopause region (80 km – 100 km) worldwide. Temperatures are derived by probing the Iron-line at 386 nm with a frequency doubled alexandrite ring laser. Beside temperature and iron density the lidar is also capable to derive stratospheric Rayleigh temperatures. Furthermore, the Fe lidar is the only lidar with negligible background at daylight because of the unique atomic physics of the Fe-line and effective spectral filtering with narrow field of view. Only a lidar with this capability can obtain temperature measurements in the polar summer mesopause region with 24 hour coverage and high resolution. After initial measurements with this new technology in 2008 – 2009, the Fe lidar was transported to Davis (68°, 79°E) in 2010. It was operated there for slightly more than two years in close collaboration with the Australian Antarctic Division (AAD). Within 2 years about 3000 hours of observations with high temporal and vertical resolution were obtained. To our knowledge no other Doppler resonance lidar has ever obtained such a large data set within only two years. This rich data set allows for the first time deep insights into the polar atmosphere at mesopause altitudes including gravity waves, tides, and chemistry.

Within MATMELT, data of this highly successful campaign with more than 1000 hours were analysed with regard to the seasonal cycle, thermal tides, and gravity waves (GWs). In particular, we discovered

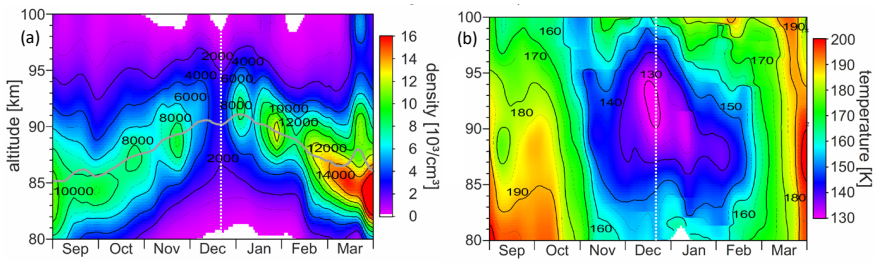

Figure 13: Seasonal evolution of (a) Fe layer and (b) temperature. The white lines indicate summer solstice. The Fe density drops significantly during the elevated mesopause.

an elevated mesopause in early summer with very cold temperatures at high latitudes - a phenomenon that occurs only in the southern hemisphere. Furthermore, our day-round lidar measurements in Antarctic summer allowed for the first time to analyse tides in temperatures and Fe densities, revealing the unexpected result that the tides have large amplitudes even in polar regions. In the following we summarize some of our main results.

2.7.2 Elevated summer mesopause

An unexpected cold mesopause at high altitudes close to summer solstice was found, but only in certain years (Morris et al., 2012; Lübken et al., 2014). We showed that large variations in the seasonal evolution of the summer polar mesopause occurred over the Antarctic which are caused by the different meteorological situations in the troposphere and stratosphere (Becker et al., 2015; Lübken et al., 2015, 2016). Figure 13 shows our averaged observations at Davis for the years with an elevated summer mesopause. The elevated mesopause occurs for a short period close to solstice and has a strong impact on tracers such as the Fe layer as well as Polar Mesospheric Summer Echoes (PMSE) and Noctilucent Clouds (NLC). For example, the altitude of maximum iron density follows the altitude of the mesopause. The elevated mesopause and the thermal state in early summer in the weeks before solstice is caused by different states of the stratospheric polar vortex varying from year to year. More precisely, fast eastward propagating gravity waves that are generated in the troposphere and responsible for the cold summer mesopause propagate to higher altitudes during years of an elevated mesopause. The corresponding coupling mechanism has become to be known as intrahemispheric coupling (e.g., Becker et al., 2015). The year-to-year variability in the southern hemisphere is related to the timing of the breakdown of the wintertime polar vortex which in some years occurs only in early summer. In years with an early breakdown of the polar vortex, the situation in the southern hemisphere is comparable to that in the northern hemisphere. The data from the summer season at Davis now serve as a benchmark for middle atmosphere GCMs.

2.7.3 Gravity waves in the stratosphere and mesosphere

The Fe lidar is also capable of measuring Rayleigh temperatures in the stratosphere. Together with resonance temperatures in the mesopause region, the GW activity is characterized in two different altitude regimes. Figure 14 shows an example of these measurements from Kaifler et al. (2015). Note, for example, the presence of upward and downward propagating phases. This indicates the presence of downward propagating GWs in the summer mesopause region. This result is unexpected but is consistent with the recent discovery of secondary GWs in the winter mesosphere (see 2.1). In summer, secondary GWs are likely generated at mesopause altitudes due to intermittency of the breakdown of fast eastward (primary) GWs. Since our rich data set covers the entire season, we determined the annual cycle of GW potential energy (Fig. 14g). Pronounced GW energy is found during winter in the stratosphere, as expected. The fact that mesopause GW energy peaks not only in summer (which is expected) but also in winter is consistent with the aforementioned pivotal importance of secondary GWs in the winter polar mesopause region.

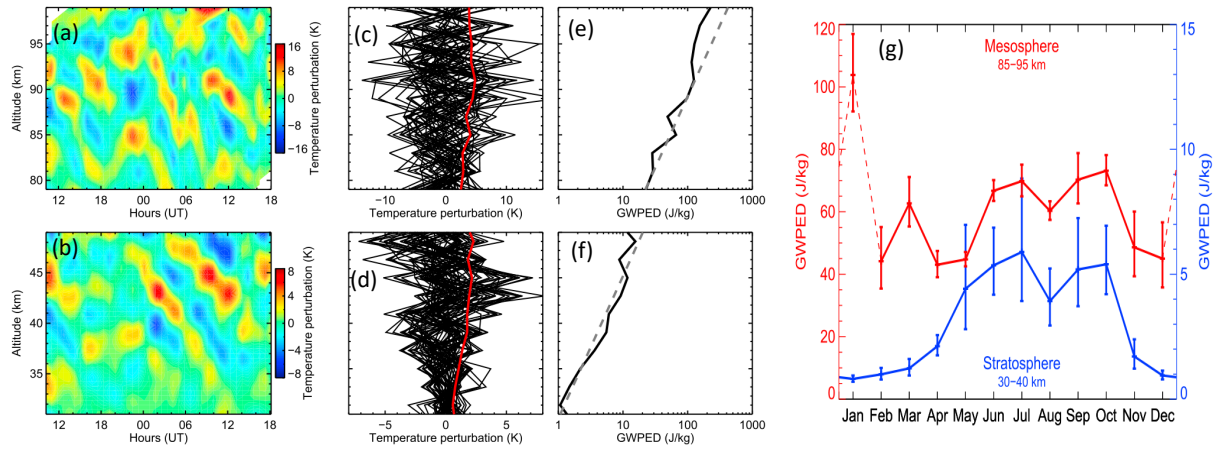

Figure 14: Illustration of GW analysis based on the lidar data: (a),(b) Keograms of GW perturbations in the stratosphere and upper mesosphere during August 15/16, 2011. (c),(d) Individual temperature profiles (black curves) and the mean temperature profile (red) that is used to derive the GW perturbations in (a),(b). (e),(f) infered profiles of the GW (available) potential energy. (g) seasonal cycle of the GW potential energy in the two altitude regimes

2.8 Thermal tides and Fe chemistry

Our measurements at Davis revealed strong thermal tides that cannot be explained by linear models (Lübken et al., 2011). We also observed strong tidal signals in Fe density, which are presumably caused by tidal effects in transport processes. Whereas temperature tides show significant variability from month to month (as expected from the seasonal cycle of the generation of tides and their propagation conditions), the phases and amplitudes of tides in iron density are remarkably persistent throughout the entire year (Fig. 15). This was not expected since the illumination by the Sun varies drastically from permanent sunshine in mid summer to absolute darkness in mid winter. Note that the metal layer cannot be considered as a passive tracer but that modifications due to chemistry play an important role. The situation is complicated by the fact that the metal layer above about 95 km is influenced by sporadic layers. Furthermore, the lower part of the metal layer shows an unexpected behavior during sunrise and sunset which will be discussed below.

The interpretation of the observed pattern in Fe density requires a model which includes the complex chemistry of the Fe layer. Currently only the Whole Atmosphere Community Climate Model (WACCM) includes metal chemistry. Simulations with the WACCM show that in case of potassium the observed tidal pattern is largely given by an altitude-dependent chemical response to the tide in background conditions (Feng et al., 2015). Whereas the potassium chemistry is known in great detail, a similar agreement between model and observations of the tidal signal in Fe density has not been achieved yet. In recent years we have therefore focussed our attention on iron chemistry.

More generally, metal layers can be observed by lidar with high temporal and spatial resolution throughout the entire year over a considerable altitude range. For the interpretation of tides and GWs as observed in metals layers, a detailed understanding of the underlying chemistry is required. Within MATMELT, the Fe chemistry was studied in cooperation with the group of Prof. John Plane (University of Leeds, UK). As part of this cooperation, the Fe chemistry was included in the WACCM model and results were compared to measurements performed with the IAP Fe lidar at Davis and also other locations. In particular, our observation of the lower edge of the Fe layer during sunrise and sunset improved our understanding of the photochemistry processes involed. The modified WACCM model can now explain the main features of the seasonal behavior of the Fe layer as shown in Fig. 13, including the suprisingly low number densities during summer. Further studies are required for a detailed understanding of the Fe layer during winter-summer transition. Some key results of these studies are published in Viehl et al. (2015a), Viehl et al. (2015b), and Viehl et al. (2016).

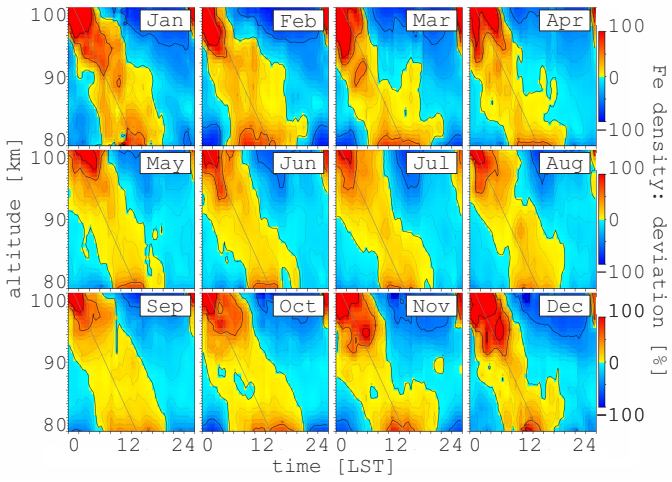

Figure 15: Tidal signal in the iron density. At higher altitudes the tide is influenced by sporadic layers. At lower altitudes the response of the metal layer to sunlight is the dominate effect.

3 Summary

The SAW project MATMELT gave rise to significant progress in our knowledge and understanding of the transport and mixing of minor constituents in the mesosphere and lower thermosphere, particulary with regard to the dynamics and nonlinear effects of gravity waves (GWs). MATMELT enhanced our modeling capabilities, as well as our techniques for ground-based observations and data analysis.

A new science topic emerged during the project: Secondary gravity waves generated in the stratopause region have large amplitudes in the winter mesopause region; they contribute to the circulation, to GW related variablity, to turbulence, and to mixing. The mixing by secondary GWs is presumably the missing link to understand the so-scalled EPP indirect effect (Sec. 2.3).

We developed a turbulence theory for the MLT by assuming that breaking GWs are subject to the scaling laws of stratified macro-turbulence (Sec. 2.2). This allowed us to estimate small-scale turbulent parameters like the integral turbulent velocity for Kolmogorov turbulence from the GW-resolving Kühlungsborn Mechanistic general Circulation Model (KMCM, Sec. 2.1). We made significant progress in developing a method to retrieve daily mean 3-dimensional wind fields and mixing coefficients in the middle atmosphere from satellite observations of temperatures and trace gases (Sec. 2.5). Furthermore, our chemistry transport model (CTM) for the MLT was extended by a comprehensive airglow model. Combining this CTM with the KMCM, we investigated the instaneous effects and the mixing due to GWs on the airglow layer (Sec. 2.4). We also made significant progress with our ground-based radar facilities, particulary reagarding our new techniques to measure 3-dimensional wind fields in the mesopause region (Sec. 2.6).
Our lidar measurement campaign at Davis (Antarctica) revealed new phenomena regarding hemispheric differences and the specific dynamics in the southern middle atmosphere, including the elevated summer mesopause, upward and downward propagating GWs in the summer mesopause region, strongly nonlinear dynamics of tides, and the dynamics of metal layers (Sec. 2.7). Some of these observational discoveries could successfully be interpreted using models and data from other instruments.

Summarizing, MATMELT was a quite successful project. We obtained many unexpected results and achieved significant technical developments that will lend support to research at IAP in the future.

References

Avsarkisov, V., E. Becker, and T. Renkwitz, 2019: Turbulent coherent structures in the middle atmosphere: Theoretical estimates deduced from a gravity-wave resolving general circulation model. *J. Geophys. Res. Atmos*, in preparation.

Avsarkisov, V. and B. Strelnikov, 2019: On the k_z^{-3} energy spectrum in strongly stratified turbulence. *J. Fluid. Mech.*, under review.

Baron, P., et al., 2013: Observation of horizontal winds in the middle-atmosphere between 30°s and 55○n during the northern winter 2009-2010. *Atmos. Chem. Phys.*, **13**, 6049–6064, doi:10.5194/acp-13-6049-2013.

Becker, E., 2009: Sensitivity of the upper mesosphere to the lorenz energy cycle of the troposphere. *J. Atmos. Sci.*, **66**, 647–666, doi:10.1175/2008JAS2735.1.

Becker, E., 2017: Mean-flow effects of thermal tides in the mesosphere and lower thermosphere. *J. Atmos. Sci.*, **74**, 2043–2063, doi:10.1175/JAS-D-16-0194.1.

Becker, E., M. Grygalashvyly, and G. R. Sonnemann, 2019: Gravity wave mixing effects on the OH*-layer. *Atmosphere*, in preparation.

Becker, E., R. Knöpfel, and F.-J. Lübken, 2015: Dynamically induced hemispheric differences in the seasonal cycle of the summer polar mesopause. *J. Atmos. Sol.-Terr. Phys.*, **129**, 128–141, doi:10.1016/j.jastp.2015.04.014.

Becker, E. and S. L. Vadas, 2018: Secondary gravity waves in the winter mesosphere: Results from a high-resolution global circulation model. *J. Geophys. Res. Atmos.*, **123**, doi:10.1002/2017JD027460.

Brune, S. and E. Becker, 2013: Indications of stratified turbulence in a mechanistic GCM. *J. Atmos. Sci.*, **70**, 231–247, doi:10.1175/JAS-D-12-025.1.

Chau, J. L., G. Stober, C. M. Hall, M. Tsutsumi, F. I. Laskar, and P. Hoffmann, 2017: Polar mesospheric horizontal divergence and relative vorticity measurements using multiple specular meteor radars. *Radio Science*, **52 (7)**, 811–828, doi:10.1002/2016RS006225, URL `http://dx.doi.org/10.1002/2016RS006225`, 2016RS006225.

Demirhan Bari, D., A. Gabriel, H. Körnich, and D. W. H. Peters, 2013: The effect of zonal asymmetries in the Brewer-Dobson circulation on ozone and water vapor distributions in the northern middle atmosphere. *Geophys. Geophys. Res. Atmos.*, **118**, 1–20, doi:10.1029/2012JD017709.

Feng, W., J. Höffner, D. R. Marsh, M. P. Chipperfield, E. C. M. Dawkins, T. P. Viehl, and J. M. C. Plane, 2015: Diurnal variation of the potassium layer in the upper atmosphere. *Geophys. Res. Lett.*, **42**, 3619–3626, doi:10.1002/2015GL063718.

Gabriel, A., 2019: Balanced and unbalanced winds of the northern winter stratosphere and mesosphere derived from satellite data. *J. Geophys. Res. Atmos*, in preparation.

Gabriel, A., H. Körnich, S. Lossow, D. H. W. Peters, J. Urban, and D. Murtagh, 2011: Zonal asymmetries in middle atmospheric ozone and water vapour derived from Odin satellite data 2001-2010. *Atmos. Chem. Phys.*, **11**, 9865–9885, doi:10.5194/acp-11-9865-2011.

Gassmann, A., 2018: Entropy production due to subgrid-scale thermal fluxes with application to breaking gravity waves. *Q. J. R. Meteorol. Soc.*, **144**, 499–510, doi:10.1002/qj.3221.

Geller, M. A., et al., 2013: A comparison between gravity wave momentum fluxes in observations and climate models. *J. Clim.*, **26**, 6383–6405, doi:10.1175/JCLI-D-12-00545.1.

Grygalashvyly, M., 2015: Several notes on the oh* layer. *Ann. Geophys.*, **33**, 923–930, doi:10.5194/angeo-33-923-2015.

Grygalashvyly, M., E. Becker, and G. R. Sonnemann, 2011: Wave mixing effects on minor chemical constituents in the mlt region: Results from a global ctm driven by high-resolution dynamics. *J. Geophys. Res.*, **116 (D18302)**, doi:10.1029/2010JD015518.

Grygalashvyly, M., E. Becker, and G. R. Sonnemann, 2012: Gravity wave mixing and effective diffusivity for minor chemical constituents in the mesosphere/lower thermosphere. *Space Sci. Rev.*, **168**, 333–362, doi:10.1007/s11214-011-9857-x.

Grygalashvyly, M., G. R. Sonnemann, P. H. F.-J. L̈bken, and U. Berger, 2014: Hydroxyl layer: Mean state and trends at midlatitudes. *J. Geophys. Res. Atmos.*, **119**, doi:10.1002/2014JD022094.

Gudadze, N., G. Stober, and J. L. Chau, 2018: Are mean vertical velocities from PMSE a good representation of mean vertical winds? *Atmospheric Chemistry and Physics Discussions*, **2018**, 1–22, doi:10.5194/acp-2018-1037.

Kaifler, N., , F.-J. Lübken, J. Höffner, R. J. Morris, and T. P. Viehl, 2015: Lidar observations of gravity wave activity in the middle atmosphere over davis (69°s, 78°e), antarctica. *J. Geophys. Res. Atmos.*, **120**, doi:10.1002/2014JD022879.

Lindborg, E., 2006: The energy cascade in a strongly stratified fluid. *J. Fluid Mech.*, **550**, 207–242.

Liu, H.-L., J. M. McInerney, S. Santos, P. H. Lauritzen, M. A. Taylor, and N. M. Pedatella, 2014: Gravity waves simulated by high-resolution Whole Atmosphere Community Climate Model. *Geophys. Res. Lett.*, **41**, doi:10.1002/2014GL062468.

Lübken, F.-J., 1997: Seasonal variation of turbulent energy dissipation rates at high latitudes as determined by in situ measurements of neutral density fluctuations. *J. Geophys. Res.*, **102**, 13 441–13 456.

Lübken, F.-J., J. Höffner, T. P. Viehl, E. Becker, R. Latteck, B. Kaifler, D. J. Murphy, and R. J. Morris, 2015: Winter/summer transition in the antarctic mesopause region at Davis (69°S). *J. Geophys. Res. Atmos.*, **120**, 12,394–12,409, doi:10.1002/2015JD023928.

Lübken, F.-J., J. Höffner, T. P. Viehl, B. Kaiffler, and R. J. Morris, 2014: Winter/summer mesopause temperature transition in 2011/2012 at Davis (69°S). *Geophys. Res. Lett.*, **41**, doi:10.1002/2014GL060777.

Lübken, F.-J., J. Höffner, T. P. Viehl, B. Kaifler, and R. J. Morris, 2011: First measurements of thermal tides in the summer mesopause region at Antarctic latitudes. *Geophys. Res. Lett.*, **38**, doi:10.1029/2011GL050045.

Lübken, F.-J., R. Latteck, E. Becker, J. Höffner, and D. J. Murphy, 2016: Using polar mesosphere summer echoes and stratospheric/mesospheric winds to explain summer mesopause jumps in antarctica. *J. Atmos. Solar-Terr. Phys.*, **162**, 106–115, doi:10.1016/j.jastp.2016.06.008.

Morris, R. J., J. Höffner, F. Lübken, T. P. Viehl, B. Kaiffler, and A. R. Klekociuk, 2012: Experimental evidence of a stratospheric circulation influence on mesospheric temperatures and ice-particles during the 2010-2011 austral summer at 69°. *J. Atmos. Sol-Terr. Phys.*, **89**, 54–61, doi:10.1016/j.jastp.2012.08.007.

Pokhotelov, D., E. Becker, G. Stober, and J. L. Chau, 2018: Seasonal variability of atmospheric tides in the mesosphere and lower thermosphere: Meteor radar data and simulations. *Ann. Geophys.*, **36 (3)**, 825–830, doi:10.5194/angeo-36-825-2018.

Randall, C. E., V. L. Harvey, D. E. Siskind, J. France, P. F. Bernath, and C. D. Boone, 2009: NO_x decent in the Arctic middle atmosphere in early 2009. *Geophys. Res. Lett.*, **36**, L18811, doi:10.1029/2009GL039706.

Reid, I. M., 2015: MF and HF radar techniques for investigating the dynamics and structure of the 50 to 110 km height region: A review. *Prog. Earth Planet. Sc.*, **2:33**, doi:10.1186/s40645-015-0060-7.

Schlutow, M., E. Becker, and H. Körnich, 2014: Positive definite and mass conserving tracer transport in spectral GCMs. *J. Geophys. Res.*, **119**, doi:10.1002/2014JD021661.

Smith, A. K., R. R. Garcia, D. R. Marsh, and J. H. Richter, 2011: WACCM simulations of the mean circulation and trace species transport in the winter mesosphere. *J. Geophys. Res.*, doi:10.1029/2011JD016083.

Stober, G. and J. L. Chau, 2015: A multistatic and multifrequency novel approach for specular meteor radars to improve wind measurements in the mlt region. *Radio Science*, **50 (5)**, 431–442, doi:10.1002/2014RS005591, URL `http://dx.doi.org/10.1002/2014RS005591`, 2014RS005591.

Stober, G., J. L. Chau, J. Vierinen, C. Jacobi, and S. Wilhelm, 2018a: Retrieving horizontally resolved wind fields using multi-static meteor radar observations. *Atmospheric Measurement Techniques Discussions*, **2018**, 1–25, doi:10.5194/amt-2018-93, URL `https://www.atmos-meas-tech-discuss.net/amt-2018-93/`.

Stober, G., S. Sommer, C. Schult, R. Latteck, and J. L. Chau, 2018b: Observation of kelvin–helmholtz instabilities and gravity waves in the summer mesopause above andenes in northern norway. *Atmospheric Chemistry and Physics*, **18 (9)**, 6721–6732, doi:10.5194/acp-18-6721-2018, URL `https://www.atmos-chem-phys.net/18/6721/2018/`.

Vadas, S. L. and E. Becker, 2018: Numerical modeling of the excitation, propagation, and dissipation of primary and secondary gravity waves during wintertime at McMurdo station in the Antarctic. *J. Geophys. Res. Atmos.*, **123**, 9326–9369, doi:10.1029/2017JD027974.

Vadas, S. L., J. Zhao, X. Chu, and E. Becker, 2018: The excitation of secondary gravity waves from local body forces: Theory and observation. *J. Geophys. Res. Atmos.*, **123**, 9296–9325, doi:10.1029/2017JD027970.

Viehl, T. P., J. Höffner, F.-J. Lübken, J. M. C. Plane, B. Kaifler, and R. J. Morris, 2015a: Summer time Fe depletion in the Antarctic mesopause region. *J. Atmos. Solar-Terr. Phys.*, **127**, 97–02, doi:10.1016/j.jastp.2015.04.013.

Viehl, T. P., J. Höffner, F.-J. Lübken, J. M. C. Plane, B. Kaifler, and R. J. Morris, 2016: Corrigendum to "Summer time Fe depletion in the Antarctic mesopause region". *J. Atmos. Solar-Terr. Phys.*, **142**, 150–151, doi:10.1016/j.jastp.2016.02.001.

Viehl, T. P., J. M. C. Plane, W. Feng, J. Höffner, B. Kaifler, and R. J. Morris, 2015b: The photolysis of FeOH and its effect on the bottomside of the mesospheric Fe layer. *Geophys. Res. Lett.*, **43**, 1373–1381, doi:10.1002/2015GL067241.

von Savigny, C., 2015: Variability of OH(3-1) emission altitude from 2003 to 2011: Long-term stability and universality of the emission rate-altitude relationship. *J. Atmos. Sol.-Terr. Phys.*, **127**, 120–128, doi:10.1016/j.jastp.2015.02.001.

Walcek, C. J., 2000: Minor flux adjustment near mixing ratio extremes for simplified yet highly accurate monotonic calculation of tracer advection. *J. Geophys. Res.*, **105**, 9335–9348.

Watanabe, S. and S. Miyahara, 2009: Quantification of the gravity wave forcing of the migrating diurnal tide in gravity wave-resolving general circulation model. *J. Geophys. Res.*, **114 (D07110)**, doi:10.1029/2008JD011218.

Wilhelm, S., G. Stober, and J. L. Chau, 2017: A comparison of 11 year mesospheric and lower thermospheric winds determined by a meteor and mf radar at 69∘n. *Ann. Geophys.*, **35**, 893–903, doi:10.5194/angeo-35-893-2017.